

B₁-Sensitivity Analysis of Quantitative Magnetization Transfer Imaging

Mathieu Boudreau,^{1*} Nikola Stikov,^{2,3} and G. Bruce Pike^{1,4}

Purpose: To evaluate the sensitivity of quantitative magnetization transfer (qMT) fitted parameters to B₁ inaccuracies, focusing on the difference between two categories of T₁ mapping techniques: B₁-independent and B₁-dependent.

Methods: The B₁-sensitivity of qMT was investigated and compared using two T₁ measurement methods: inversion recovery (IR) (B₁-independent) and variable flip angle (VFA), B₁-dependent). The study was separated into four stages: 1) numerical simulations, 2) sensitivity analysis of the Z-spectra, 3) healthy subjects at 3T, and 4) comparison using three different B₁ imaging techniques.

Results: For typical B₁ variations in the brain at 3T (±30%), the simulations resulted in errors of the pool-size ratio (F) ranging from −3% to 7% for VFA, and −40% to >100% for IR, agreeing with the Z-spectra sensitivity analysis. In healthy subjects, pooled whole-brain Pearson correlation coefficients for F (comparing measured double angle and nominal flip angle B₁ maps) were $\rho = 0.97/0.81$ for VFA/IR.

Conclusion: This work describes the B₁-sensitivity characteristics of qMT, demonstrating that it varies substantially on the B₁-dependency of the T₁ mapping method. Particularly, the pool-size ratio is more robust against B₁ inaccuracies if VFA T₁ mapping is used, so much so that B₁ mapping could be omitted without substantially biasing F. *Magn Reson Med* 000:000–000, 2017. © 2017 International Society for Magnetic Resonance in Medicine.

Key words: quantitative magnetization transfer; B₁ mapping; T₁ mapping; sensitivity analysis

INTRODUCTION

Quantitative magnetization transfer (qMT) imaging is a powerful MRI technique used to investigate macromolecular content not typically detectable with conventional MRI. MR properties of macromolecular hydrogen are measured with qMT by indirect means: the magnetization of the macromolecular pool is saturated, and energy is exchanged with nearby water molecules via cross-relaxation processes and chemical exchange (1,2). In

imaging brain white matter (WM), the pool-size ratio (F), the ratio between the equilibrium magnetization of hydrogen in macromolecules versus hydrogen in water, has been shown to be a good marker of myelin density (3,4). In particular, the pool-size ratio has been used to study multiple sclerosis lesions (5–7). Several methods have been developed to estimate qMT parameters from the mathematical model that describes the exchange processes (8–12).

Commonly, off-resonance qMT imaging uses a magnetization transfer (MT)-prepared spoiled gradient (SPGR) echo pulse sequence (13). It is a standard SPGR sequence preceded by an off-resonance radiofrequency (RF) pulse that varies in amplitude and frequency offset between measurements; 10 measurements or more are generally required to fit this Z-spectrum (normalized MT signal vs. off-resonance frequencies) (14), and one additional measurement without the MT-preparation for signal normalization. These qMT techniques also require three additional measurements: B₀, B₁, and T₁. In postprocessing, B₀ maps calibrate the off-resonance frequency of the MT pulse in each voxel. B₁ maps are used to scale the SPGR excitation flip angle and MT-pulse saturation power. A T₁ map is necessary to constrain certain fitting parameters of the two-pool MT fitting model (2). For a given voxel, the measured T₁ (T_{1,meas}) is a function of the T₁ of the water molecules (T_{1,f}, “f” is for “free pool”) and of the T₁ of the macromolecules (T_{1,r}, “r” is for “restricted pool”), and two other parameters (F, ratio of the two pool sizes in the voxel, and k_f, the exchange rate constant). The large number of measurements required to sample the Z-spectrum and additional quantitative maps make qMT a time-costly technique.

Increasingly, whole-brain qMT imaging has been achieved via a reduction in qMT measurements (15,16) and new rapid techniques to measure the required quantitative calibration maps (17–19). However, integrating new methods into quantitative imaging studies can introduce unintended effects. For example, transitioning from single-slice T₁ mapping techniques (i.e., inversion recovery [IR]) to three-dimensional [3D] techniques, variable flip angle [VFA]) also results in transitioning from B₁-insensitive (20,21) to B₁-sensitive (22) T₁ mapping. If VFA is used in the qMT imaging protocol, inaccuracies in B₁ will propagate into fitted qMT parameters through two pathways instead of just one (Fig. 1): from errors induced in T₁, used to restrict the fitting parameters, and from errors in scaling the MT saturation powers with the B₁ maps. The potential effect of B₁-uncorrected qMT on the fitted parameters has been noted in previous work (23,24); however, these were limited in scope to B₁-insensitive T₁ techniques. To our knowledge, no comprehensive characterization of the B₁-

¹McConnell Brain Imaging Centre, Montreal Neurological Institute, McGill University, Montreal, Quebec, Canada.

²Département du Génie Biomédical, École Polytechnique de Montreal, Montreal, Quebec, Canada.

³Montreal Heart Institute, Montreal, Quebec, Canada.

⁴Hotchkiss Brain Institute and Department of Radiology, University of Calgary, Calgary, Alberta, Canada.

*Correspondence to: Mathieu Boudreau, MSc, McConnell Brain Imaging Centre, Room WB-325, Montreal Neurological Institute, McGill University, Montreal, Quebec H3A 2B4, Canada. E-mail: mathieu.boudreau2@mail.mcgill.ca

Received 28 November 2016; revised 2 February 2017; accepted 17 February 2017

DOI 10.1002/mrm.26673

Published online 00 Month 2017 in Wiley Online Library (wileyonlinelibrary.com).

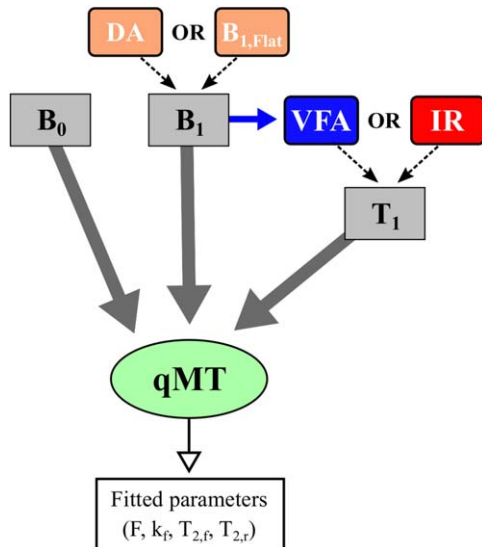


FIG. 1. Quantitative measurements used in our magnetization transfer (MT)-prepared spoiled gradient quantitative MT study. Solid arrows are used for required measurements; dotted arrows are used for specific methods of a particular measurement. The double angle (DA) method is an explicitly measured B_1 map. $B_{1,Flat}$ maps are generated using a single value in all voxels. Variable flip angle (VFA) is a T_1 mapping methods that also requires B_1 as a support measurement, unlike inversion recovery (IR).

sensitivity of qMT (and notably, comparing different T_1 mapping methods) has previously been performed.

This work focuses on answering the following three questions: 1) How sensitive is each qMT parameter to B_1 -inaccuracies? 2) How does the B_1 -sensitivity of qMT parameters differ between protocols using B_1 -independent (IR) and B_1 -dependent (VFA) T_1 mapping methods?; and 3) Which T_1 mapping method results in the most robust measure of the pool-size ratio in the presence of B_1 -inaccuracies? To explore these questions, we first focused on simulations under ideal measurement conditions for a single tissue type, and then used this framework to perform a sensitivity analysis of the signal curves. We then measured qMT maps in healthy human volunteers using both T_1 mapping methods (IR and VFA), and compared measured B_1 maps with fictitious maps generated to have a large range of potential inaccuracies. Finally, we compared the relative agreement of qMT fits between three different B_1 mapping methods (double angle, actual flip angle imaging, Bloch-Siegert) using both T_1 mapping methods (IR and VFA).

METHODS

All measurements were performed with a 3.0 T whole-body MRI scanner (Magnetom TIM TRIO; Siemens, Erlangen, Germany) using a 32-channel phased-array receive-only head coil and whole-body transmit coil. Healthy volunteers were scanned after providing informed consent, in compliance with and approved by the institutional ethics committee. The total scan time for the entire acquisition protocol described in the B_1 -Sensitivity of qMT in Healthy Subjects and B_1 Method Comparison sections was 28 minutes and 58 seconds.

Simulations

The coupled Bloch-McConnell differential equations describing two-pool magnetization exchange were solved numerically (MATLAB 2011a; MathWorks Inc., Natick, MA) for a pulsed MT-prepared SPGR pulse sequence using the Sled and Pike model (23,25). The pulse sequence was decomposed into event blocks of instantaneous saturation of the free pool, constant irradiation of the restricted pool, and free precession. Prior to simulating exchange, the fractional saturation of the longitudinal magnetization induced by direct saturation was computed numerically in the absence of exchange and T_1 recovery. The steady-state solution was approximated analytically using the assumption that the magnetization at an arbitrary time t should be equal to that of time $t + \text{repetition time (TR)}$, as described in detail in the appendix of Sled and Pike (10). The signal was simulated with the following pulse sequence parameters (14,15): $\text{TR} = 25$ ms, excitation flip angle (FA) = 7° , MT pulse flip angle = 142° and 426° , MT pulse duration = 10 ms, 10 off-resonance frequencies ranging between 423.9 Hz and 17.2354 kHz in logarithmic steps. The envelope of the MT-preparation RF pulse was a Gaussian-Hanning function, and a super-Lorentzian lineshape function was used for the transition rate of the restricted pool to approximate the behavior observed in tissues (25). qMT tissue parameters for all simulations were set to healthy white matter values measured in a previous scan: $F = 0.122$ n.u. (normalized units), magnetization exchange rate (k_f) = 3.97 s $^{-1}$, free-pool longitudinal relaxation rate ($R_{1,f} \equiv 1/T_{1,f}$) = 1.12 s $^{-1}$, restricted-pool longitudinal relaxation rate ($R_{1,r} \equiv 1/T_{1,r}$) = 1.00 s $^{-1}$, free-pool transverse relaxation time ($T_{2,f}$) = 27.2 ms, restricted-pool transverse relaxation time ($T_{2,r}$) = 10.96 μ s.

SPGR qMT experiments require three additional quantitative measures: B_0 , B_1 , and T_1 . B_0 measurement methods typically do not require B_1 or T_1 calibration; thus, ideal B_0 homogeneity was used in the simulations. MT signal values were simulated using B_1 (to scale the MT saturation powers and excitation flip angles) and $T_{1,meas}$ (to constrain the fitting parameters) that were fixed to their ideal values (1 n.u. and 0.9 s respectively). The MT signal was subsequently fitted using the Sled and Pike method (23). As per convention, $R_{1,r}$ was fixed to 1 s $^{-1}$. $R_{1,f}$ was calculated during the fitting algorithm from an analytical expression of F , k_f , $R_{1,r}$, and $T_{1,meas}$. To investigate the effect of inaccuracies in B_1 and $T_{1,meas}$ on the fitted qMT parameters, the simulated MT signal values were fitted using a large range of B_1 and $T_{1,meas}$ values. Four qMT parameters (F , k_f , $T_{2,f}$, $T_{2,r}$) were explicitly fitted for each pair of 100 B_1 and 100 $T_{1,meas}$ values (10,000 combinations). The set of B_1 values varied linearly from 0.5 to 2 n.u., and $T_{1,meas}$ varied from 0.1 s to 4 s. For this stage, B_1 and $T_{1,meas}$ varied independently of each other.

We investigated the qMT parameter sensitivities due to B_1 inaccuracies for two T_1 mapping techniques: IR, approximately B_1 independent (21), and VFA, inherently B_1 -dependent (22). The IR case was interpreted to be a linear subset of the B_1 - T_1 combination discussed above by a fixed T_1 ($T_{1,IR} = 0.9$ s, constant). The VFA signals from a two flip angle experiment were calculated for

$T_1 = T_{1,\text{true}} = 0.9$ s from the analytical steady-state SPGR equation ($\text{TR} = 25$ ms, $\text{FA} = 3^\circ$ and 20°). $T_{1,\text{VFA}}$ values were subsequently estimated by linear least-square fitting of the VFA data with flip angle calibration (26) using the set of 100 B_1 values (0.5 to 2 n.u.). The fitted VFA $T_{1,\text{meas}}$ values were then used in conjunction with their respective B_1 values to fit the qMT parameters to the simulated MT signal.

Sensitivity Analysis

To provide further insight into the behavior of fitted parameters in the presence of B_1 inaccuracy, a sensitivity analysis of the qMT signal was performed (27). For each qMT parameter, the following definition of sensitivity was used (cf. Appendix A):

$$S_{p,i} \equiv \frac{\Delta M_i}{\Delta p}, \quad p = F, k_f, T_{2f}, T_{2r}, B_1 \quad [1]$$

where the index i describes a specific qMT acquisition point, M_i is the normalized signal of the i^{th} qMT measurement, and $S_{p,i}$ is the sensitivity of the MT signal with respect to p for the i^{th} qMT acquisition. The sensitivity $S_{p,i}$ represents the change in normalized MT signal induced by a slight change in fitting parameter value or model input value (e.g., B_1). A large absolute $S_{p,i}$ value signifies that, to a linear approximation, a large change in MT signal will occur (at that Z-spectrum value) for a small variation of p . In the context of fitting data to measurements using an inaccurate B_1 value, the following relationship can be shown (cf. Appendix A):

$$\sum_{p \neq B_1} S_{p,i} \Delta p \cong -S_{B_1,i} \Delta B_1 \quad [1]$$

Thus, the sensitivity values can provide an insight as to why certain fitting parameters are more likely to have large errors due to inaccurate B_1 values. When comparing two measurement protocols, the following metrics can be expected to provide insight into which fitting parameters p are more/less sensitive to B_1 inaccuracies (cf. Appendix A):

$$|\hat{S}_p \cdot \hat{S}_{B_1}| \quad [3]$$

$$\frac{B_1 \|\mathbf{S}_{B_1}\|}{p \|\mathbf{S}_p\|} \quad [4]$$

where \mathbf{S} is the vector of sensitivity values for a set of N measurements, $\|\mathbf{s}\|$ is its norm, and $\hat{\mathbf{S}}$ is its unit vector. If the sensitivity values of a parameter p and B_1 have very similar curves (Eq. [3] ≈ 1), then p is likely to be most sensitive to B_1 inaccuracies compared to other parameters. The relative error of p will then be proportional to the ratio in Eq. [4].

The qMT measurement protocol and tissue parameters from the Simulations section were used to simulate normalized MT signal values. Partial derivatives with respect to qMT parameters (and B_1) of the MT signal were evaluated at each point of the Z-spectrum (28). B_1 sensitivity values were calculated for two cases: $T_{1,\text{meas}}$ independent of B_1 (which for consistency with the other sections we designate as IR), and $T_{1,\text{meas}}$ with VFA

B_1 -dependency. As $T_{1,\text{meas}}$ is primarily used to constrain R_{1f} , R_{1f} was modified in addition to B_1 accordingly for the VFA case. The derivative steps were fixed to a $10^{-5}\%$ relative increase of the parameter denominator value, sufficient for the convergence of the partial derivative at each Z-spectrum point of our qMT protocol.

B₁-Sensitivity of qMT in Healthy Subjects

Three healthy adult volunteers were scanned (two males, one female, 30 ± 4 years old). All quantitative imaging sequences were acquired at a resolution of $2 \times 2 \text{ mm}^2$ in-plane $\times 5 \text{ mm}$ slice thickness. Single slices were acquired parallel to the anterior commissure–posterior commissure (AC-PC) line, superior to the corpus callosum.

T_1 Maps

VFA T_1 maps were acquired using a spoiled 3D gradient echo sequence (19): echo time (TE) = 2.89 ms, TR = 15 ms, FA = 3° and 20° , spoiler gradient moment (A_G) = 280 mT · ms/m, RF phase increment (ϕ) = 169° , 1 m 28 s scan time. Prior to fitting the data for T_1 , the nominal flip angles were scaled voxel-wise with each B_1 map. The VFA T_1 values were then estimated from linear least-square fitting. Inversion recovery T_1 data were collected from a four-inversion-time (TI) spin-echo sequence (21): TE/TR = 11/1550 ms, TI = 30, 530, 1030, 1530 ms, 9 m 16 s scan time. An open-source software package for robust inversion recovery fitting was used to fit the IR T_1 maps (20).

qMT Maps

qMT data were acquired according to the 10-point MT-prepared SPGR acquisition protocol described in the Simulations methods section, which for our single slice has a 2 m 38 s scan time. B_0 maps were acquired for off-resonance frequency correction using a two-point phase-difference gradient measurement (29): TE1/TE2/TR = 4/8.48/25 ms, FA = 7° , 30 s scan time. qMT parameter maps were produced by fitting the normalized qMT data voxel-wise using the Sled and Pike fitting model (30).

B_1 Maps

Two categories of B_1 maps were compared: 1) in vivo measured B_1 maps and 2) B_1 maps that had a single value assigned to all voxels ($B_{1,\text{Flat}}$). $B_{1,\text{Flat}}$ maps were used to investigate the sensitivity of qMT to B_1 inaccuracies for in vivo conditions (e.g., noise, tissue partial volume, a broad range of qMT tissue parameter values). Single-slice double angle (DA) B_1 maps ($B_{1,\text{DA}}$) were acquired using a spin-echo readout: TE/TR 12/1550 ms, FA = $60^\circ/120^\circ$, with slice-selective excitation and 180° refocusing pulses, 4 m 28 s scan time. A set of $B_{1,\text{Flat}}$ maps were generated for a range of values ($B_{1,\text{Flat}} = 0.5, 0.75, 0.9, 1, 1.1, 1.25, 1.5, 2$ n.u.), where $B_{1,\text{Flat}} = 1$ n.u. represents the nominal flip angle case. Prior to fitting the qMT data, each B_1 map ($B_{1,\text{DA}}$ and the set of $B_{1,\text{Flat}}$) was used as a corrective factor for the VFA nominal flip angles, MT excitation flip angles, and MT saturation powers.

Data Analysis

qMT parameter maps (F , k_f , $T_{2,f}$, $T_{2,r}$) were fitted voxel-wise using four sets of B_1 and T_1 combinations: $B_{1,DA}$ and $B_{1,Flat}$ used with IR and VFA T_1 maps (Fig. 1). Voxel data of each qMT parameter map were pooled (across all subjects) for each B_1 and T_1 set, and linear regression analysis was performed (comparing $B_{1,DA}$ and each $B_{1,Flat}$).

B_1 Method Comparison

Several techniques exist to measure B_1 maps, and each method can be prone to unique sources of systemic biases or local artifacts (31). To probe the robustness of the B_1 -sensitivity of qMT between different B_1 measurement techniques, two additional B_1 maps were acquired and compared against the DA B_1 maps in all three subjects from the B_1 -Sensitivity of qMT in Healthy Subjects section. Actual flip angle imaging (AFI) (17), a two-TR steady-state SPGR-based pulse sequence, was applied to produce B_1 maps with a $2 \times 2 \times 5 \text{ mm}^3$ whole-brain 3D spoiled acquisition (19): TE/TR1/TR2 3.53/20/100 ms, FA = 60° , $A_G = 450 \text{ mT} \cdot \text{ms/m}$, $\phi = 39^\circ$, 5 m 38 s scan time. Bloch-Siebert shift (BS) B_1 mapping (18), an SPGR-based method with an off-resonance RF preparation pulse, produced B_1 maps using a single-slice $2 \times 2 \times 5 \text{ mm}^3$ acquisition: TE/TR 15/100 ms, $\alpha = 25^\circ$, 8 ms Fermi Pulse of 500° at $\pm 4 \text{ kHz}$ off-resonance, phase-shift constant (K_{BS}) = 74.01 rad/G^2 , 19 s scan time.

At the resolution of our data ($2 \times 2 \times 5 \text{ mm}^3$), partial volume effects near cortical grey matter (GM) and adjacent to ventricles can be significant. The partial volume effects can make the analysis of in GM challenging. Preliminary data (not shown) suggested that an insufficient number of voxels exist containing only GM, for a reliable analysis to be performed, and including all voxels containing at least some GM would include a significant bias in the qMT parameters from cerebrospinal fluid (CSF). As such, the images were masked solely for WM. Whole-brain T_1 -weighted magnetization-prepared rapid gradient-echo (MP-RAGE) 3D volumes ($1 \times 1 \times 1 \text{ mm}^3$) were acquired: TE/TR/TI = 3.32/2300/900 ms, parallel imaging acceleration factor = 2, bandwidth (BW) = 230 Hz/Px , 5 m 30 s scan time. Tissue classification maps (WM, GM, CSF) were estimated via Intensity Normalized Stereotaxic Environment for the Classification of Tissue (32) using the MP-RAGE data with the International Consortium for Brain Mapping-152 atlas. WM tissue masks were resampled to match the AC-PC $2 \times 2 \times 5 \text{ mm}^3$ single slices using a majority voting analysis (75% threshold). The histograms of WM qMT parameters were calculated for all three B_1 maps, using both VFA and IR T_1 maps in the processing pipeline. Chi-square (χ^2) of the histogram differences was calculated to quantify how well the histograms matched between the DA case versus AFI and BS.

RESULTS

Simulations

The error (%) in F calculated after fitting the simulated qMT signal using each B_1 and T_1 value-pair is displayed in Figure 2. T_1 curves as a function of B_1 inaccuracies are superimposed with solid (IR) and dotted (VFA) lines. The error in F (%) is a smooth nonlinear function of B_1

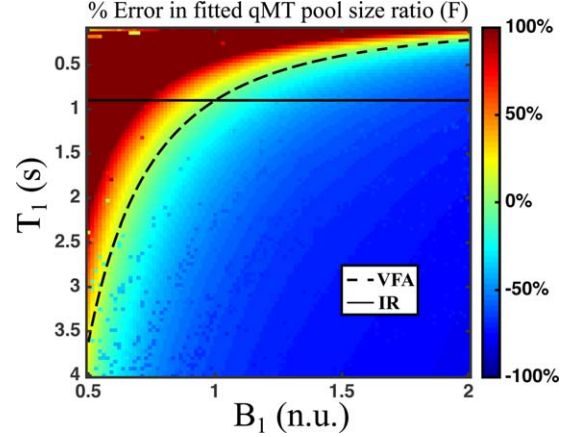


FIG. 2. Simulated differences (%) in fitted quantitative magnetization transfer (qMT) F values in the presence of a wide range of B_1 and T_1 errors ($B_{1,true} = 1 \text{ n.u.}$, $T_{1,true} = 0.9 \text{ s}$). The superimposed lines plot the T_1 distribution for a B_1 -independent T_1 mapping method (inversion recovery [IR], solid line, and variable flip angle [VFA], dashed line). n.u. = normalized units.

and T_1 , with some speckling in values occurring far from the true B_1 and T_1 intersection (where they are both grossly inaccurate). IR T_1 is set to be constant, resulting in a wide range of errors in F ($< -100\%$ to 50%) for the B_1 inaccuracy range evaluated. B_1 underestimation resulted in an overestimation of VFA T_1 , and the error in F for this case overlaps near the 0% error contour line (green).

At 3 T , the B_1 amplitude varies approximately $\pm 30\%$ in the brain. The errors in the four qMT fitted parameters are shown for this range of B_1 inaccuracy in Figure 3, for both the IR and VFA T_1 cases. Note that Figure 3a corresponds to the values superimposed by the IR and VFA T_1 lines in Figure 2. Relative to IR, errors in F due to B_1 inaccuracies are substantially reduced using VFA. For VFA, the errors in F ranged between -3% and 7% (blue line) for $\pm 30\%$ B_1 inaccuracy; for IR, the errors ranged between -40% and $>100\%$ (red line). k_f exhibits the inverse trend; errors in k_f are larger for VFA relative to IR (Fig. 3b) for all B_1 values. No advantage in either T_1 method is identified for $T_{2,f}$; the slopes of the curves flip between both T_1 methods with approximately the same magnitude. $T_{2,r}$ is insensitive to B_1 inaccuracies for both T_1 mapping method (Fig. 3d).

For IR, a 10% underestimation in B_1 produced a 23% error in F , 6% error in k_f , 12% error in $T_{2,f}$, and 0.78% error in $T_{2,r}$. For VFA, a 10% underestimation in B_1 produced a 1.5% error in F , 25% error in k_f , 6.7% error in $T_{2,f}$, and 0.78% error in $T_{2,r}$. Thus, switching from IR to VFA reduces B_1 -sensitivity of F by a factor of 15 for a 10% error in B_1 . The error in F for the IR case (23%) produced from a 10% error in B_1 is consistent with the value calculated by Sled and Pike using a 60-point protocol (20%) (23).

Sensitivity Analysis

The plots of the sensitivity values for our qMT protocol are shown in Figure 4, and the sensitivity metrics (from Eqs. [3] and [4]) are calculated in Table 1. The curve similarity metric $|\hat{S}_p \cdot \hat{S}_{B_1}|$ informs us of how well changing a particular fitting parameter p (F , k_f , $T_{2,f}$, and $T_{2,r}$) can correct the

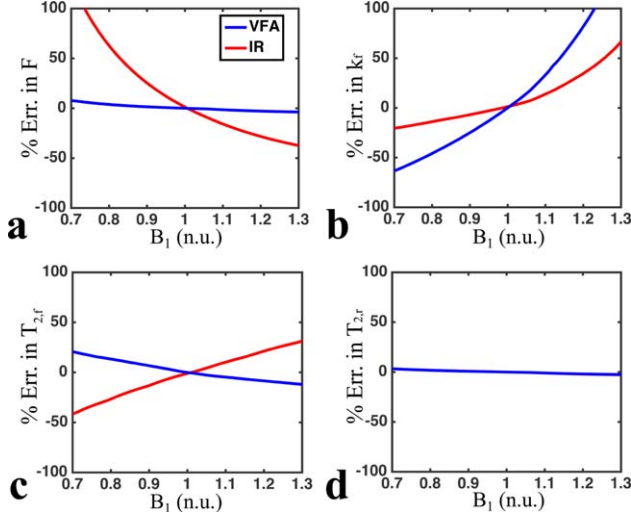


FIG. 3. Simulated errors (%) in fitted quantitative magnetization transfer (qMT) parameters for $\pm 30\%$ B_1 errors (a: pool size ratio $[F]$, b: magnetization exchange rate $[k_f]$, c: free pool T_2 $[T_{2,f}]$, d: restricted pool T_2 $[T_{2,r}]$). Fits using a B_1 -independent T_1 measure (inversion recovery [IR]) are shown in red, and those using variable flip angle (VFA) T_1 mapping are shown in blue. The IR curve in d) is underneath the VFA line. Note: The solid and dashed lines in Figure 2 to show the dependence of IR and VFA T_1 on B_1 . n.u. = normalized units.

expected signal change due to an error in B_1 . For a B_1 -independent T_1 measurement (e.g., IR), we see from Table 1 that the $|\hat{S}_p \cdot \hat{S}_{B_1}|$ values have the following trend: $(F \approx 1) > k_f > T_{2,f} \gg T_{2,r}$; for VFA: $(k_f \approx 1) > F \approx T_{2,f} \gg T_{2,r}$. This suggests that F has a higher sensitivity to B_1 inaccuracies for IR than VFA, with a reverse relationship expected for k_f , both in agreement with the simulations results from the Simulations section. Figure 4 illustrates these relationships; the sensitivity curves for B_1^{IR} (Fig. 4a) have a similar pattern to those for F (Fig. 4c), whereas the sensitivity curves for B_1^{VFA} (Fig. 4b) have a similar pattern to those for k_f (Fig. 4d). For these respective cases, $\frac{B_1 \|\hat{S}_{B_1}\|}{\rho \|\hat{S}_p\|}$ is greater for k_f than F (Table 1), suggesting that larger relative errors in k_f are required to compensate B_1^{VFA} inaccuracies than F for B_1^{IR} , consistent with our simulation observations. Lastly, note that the minima observed in $|\mathcal{S}_{T_{2,r}}|$ is due to a zero-crossing of $\mathcal{S}_{T_{2,r}}$, a characteristic that was also reported in a previous study (33).

B₁-Sensitivity of qMT in Healthy Subjects

Noise, partial volume effects of tissue, and a wide range of different qMT tissue parameters were not considered in the previous sections, all of which could potentially impact the B_1 -sensitivity of the qMT fits. In vivo data were acquired to investigate whether the B_1 -sensitivity features identified in our simulations hold under real-world conditions. Single-slice qMT parameter maps are shown in Figure 5, fitted using VFA (a) and IR (b), for either DA B_1 maps or the nominal flip angle assumption ($B_{1,Flat} = 1$). For VFA and $B_{1,Flat}$, the elevated T_1 at the center of the brain counteracts the underestimated B_1 values, resulting in minimal errors in the qMT F maps relative to the IR F maps. At the perimeter of the brain where $B_{1,Flat}$

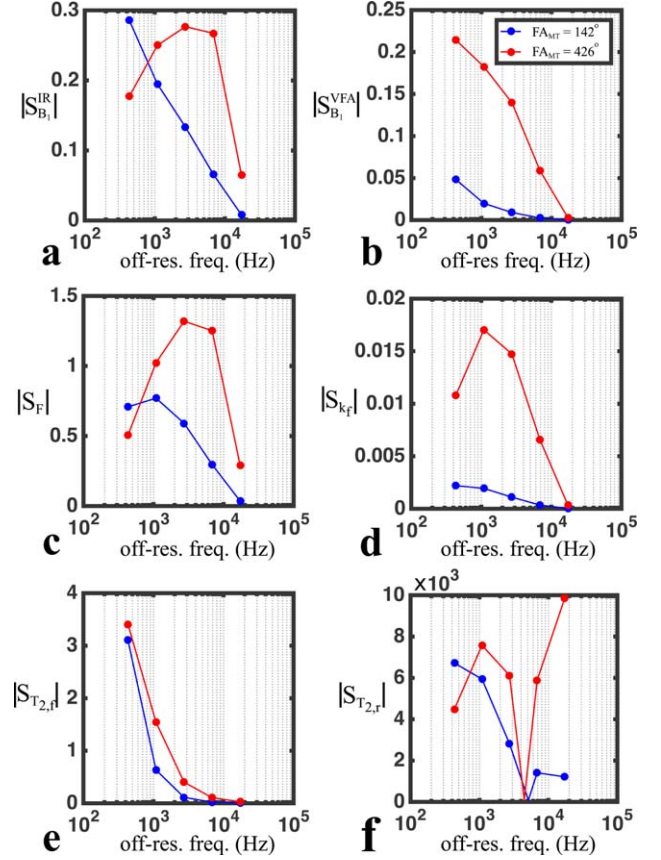


FIG. 4. Sensitivity analysis of the magnetization transfer signal relative to B_1 (a, b) and fitting variables (c-f). The plots (note scale changes) show the magnitudes of the sensitivity values (Eq. [2]).

overestimates the measured values, the VFA case results in nearly no qMT F bias. Regions of very high T_1 , suggesting presence of CSF, do exhibit speckling of large errors in F . qMT F fitted with the combination of IR and $B_{1,Flat}$ resulted in large errors, where the B_1 profile is clearly distinguishable in map of errors in F .

Table 2 lists the correlation and linear regression slope ($B_{1,DA}$ vs. $B_{1,Flat} = 1$) for all fitted qMT parameters, using both T_1 methods. qMT F using VFA had the best correlation ($\rho = 0.97$, slope = 0.97), as opposed to IR ($\rho = 0.81$, slope = 0.57). $T_{2,f}$ also demonstrated good correlations

Table 1

qMT Z-Spectra Sensitivity Comparison Metrics for B_1 (Accounting for the B_1 -Sensitivity of Each T_1 Method, IR, and VFA) and Each Fitted qMT Parameter

	$ \hat{S}_p \cdot \hat{S}_{B_1} $		$\frac{B_1 \ \hat{S}_{B_1}\ }{\rho \ \hat{S}_p\ }$	
	$S_{B_1}^{IR}$	$S_{B_1}^{VFA}$	$S_{B_1}^{IR}$	$S_{B_1}^{VFA}$
S_F	0.975	0.754	2.05	1.07
S_{k_f}	0.815	0.951	6.02	3.12
$S_{T_{2,f}}$	0.704	0.776	4.67	2.43
$S_{T_{2,r}}$	0.482	552	3.08	1.61

Note: $S_{B_1}^{IR}$ corresponds to the qMT sensitivity values relative to B_1 assuming a B_1 -independent measure of T_1 , whereas $S_{B_1}^{VFA}$ considers a qMT protocol using a VFA T_1 measurement, which inherently is B_1 -dependent. IR = inversion recovery; qMT = quantitative magnetization transfer; VFA = variable flip angle.

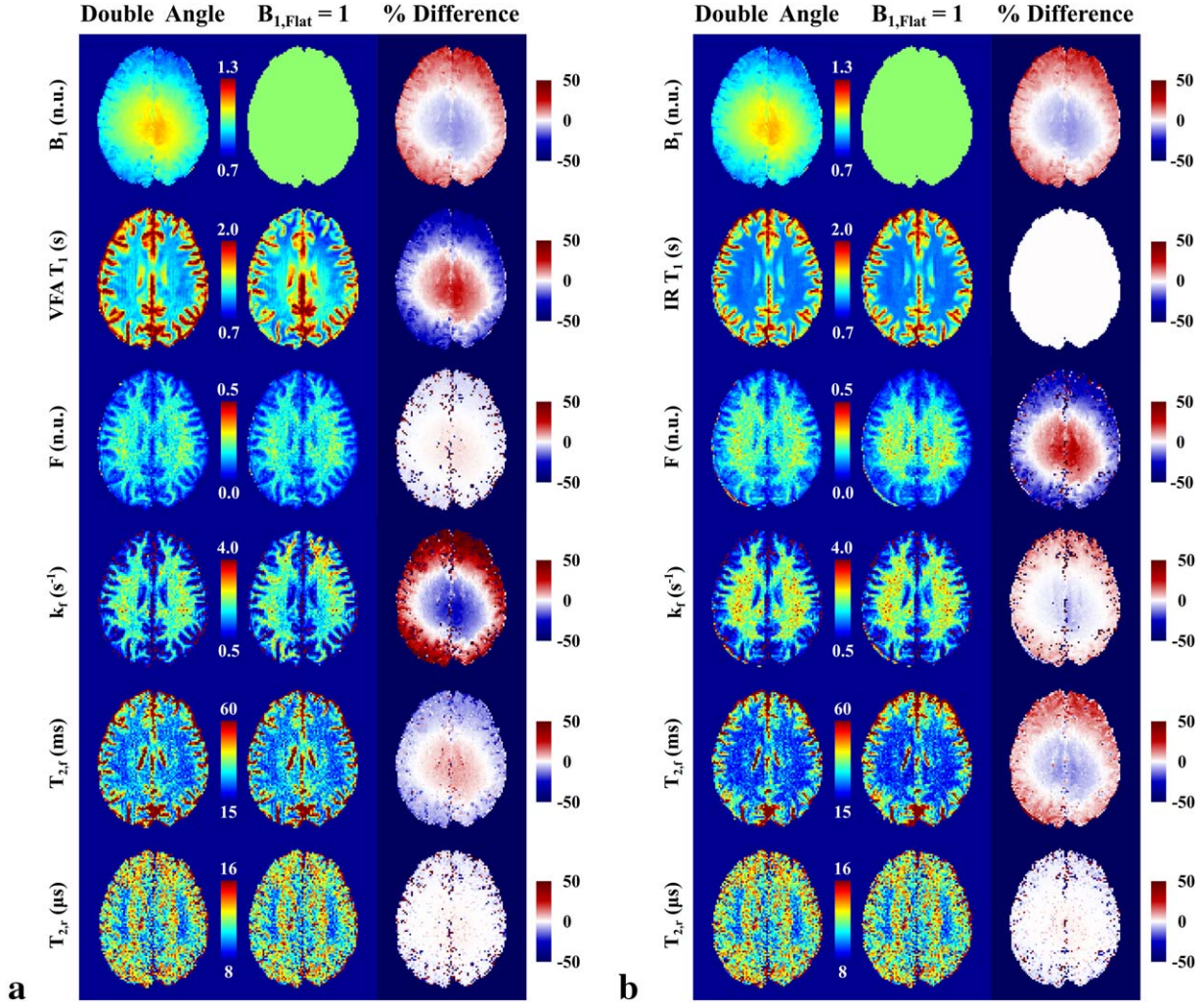


FIG. 5. Single-subject comparison of quantitative magnetization transfer parameter maps fitted using double angle and $B_{1,Flat} = 1$ maps using (a) variable flip angle (VFA) T_1 maps corrected using the corresponding B_1 map, and (b) inversion recovery (IR) T_1 maps independent of B_1 .

($\rho = 0.97$), but with an underestimation of the slope (slope = 0.86). Based on our simulations, the low correlation of k_f for the IR case ($\rho = 0.26$) was unexpected. Upon further investigation of the raw k_f scatter plots (not shown), the linear assumption for fitting the k_f scatter plot was violated. Thus, for conditions exhibited in vivo (i.e., noise, multi-tissue voxels), the k_f parameter fits

were not stable in the presence of large B_1 errors, resulting in k_f voxel values diverging substantially in the scatter plot data.

Expanding the correlation analysis of F to a larger $B_{1,Flat}$ set of values (ranging from 0.5 to 2 n.u.), F was more robust against B_1 overestimations than underestimations (Fig. 6a). The correlations break down rapidly for $B_{1,Flat}$ values below 0.75, yet are near unity for most values ranging between 1 and 2. The same trend is true for the fit slope for F ; it is near unity for slight B_1 underestimations and for large B_1 overestimations (Fig. 6b).

Table 2
Pooled (All Subjects) Pearson Correlation Coefficients and Linear Regression Slopes for qMT Values Comparing Measured DA B_1 Maps and Fictitious $B_{1,Flat} = 1$ Maps^a

qMT	(B _{1,DA}) vs. (B _{1,Flat} = 1)			
	T _{1,VFA}		T _{1,IR}	
	Pearson ρ	Slope	Pearson ρ	Slope
F	0.97	0.97	0.81	0.57
k_f	0.27	0.24	0.26	0.25
$T_{2,f}$	0.97	0.86	0.93	0.90
$T_{2,r}$	0.81	0.78	0.89	0.82

^a $B_{1,Flat} = 1$ is equivalent to the nominal flip angle assumption DA = double angle; qMT = quantitative magnetization transfer.

B₁ Mapping Method Comparison

Three B_1 maps (DA, AFI, BS) are shown for one subject in Figure 7. The DA B_1 map, which was used in the previous section, was set as the reference measurement that the two other methods are compared against. AFI and BS displayed heterogeneous inaccuracy patterns relative to DA; voxel-wise relative errors were $\pm 10\%$. In this subject, B_1 in the frontal lobe was overestimated by both methods, whereas the left and right posterior regions

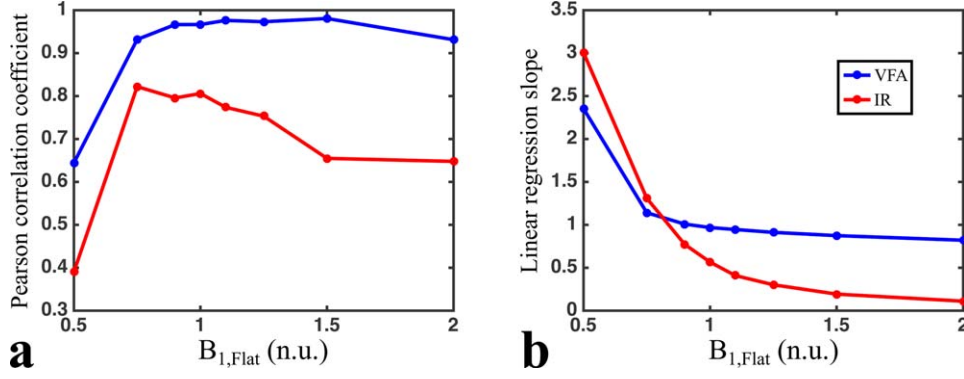


FIG. 6. Pooled (all subjects, voxel-wise) whole brain Pearson correlation coefficients **(a)** and linear regression slopes **(b)** for qMT F values between the measured double angle B_1 maps and generated $B_{1,Flat}$ maps. IR=inversion recovery; n.u.=normalized units; VFA=variable flip angle.

showed different bias patterns for both techniques. Relative to DA, the voxelwise Pearson correlation and linear regression coefficients for all three subjects were $\rho = 0.904$ ($y = 1.035x - 0.034$) for BS and $\rho = 0.912$ ($y = 0.960x + 0.038$) for AFI. Despite variations in voxel-wise accuracy between B_1 methods, the histograms of WM qMT F matched very well for the VFA case (Fig. 8b, same subject as Fig. 7). The excellent overlap of histogram curves for this case resulted in low χ^2 values for this subject ($\chi^2_{AFI} = 1.24$, $\chi^2_{BS} = 1.41$), unlike to the IR case for F ($\chi^2_{AFI} = 5.45$, $\chi^2_{BS} = 6.40$). Consistent with our simulations, the inverse relationship was true for k_f in WM (Fig. 8c,d). The mean χ^2 values of F for all subjects also had low standard deviations for VFA ($\chi^2_{BS} = 1.24 \pm 0.33$, $\chi^2_{BS} = 1.41 \pm 0.12$) relative to IR ($\chi^2_{AFI} = 9.25 \pm 5.81$, $\chi^2_{BS} = 9.17 \pm 3.94$; Fig. 8a). For k_f , the means for all subject for VFA were $\chi^2_{AFI} = 6.10 \pm 1.81$, $\chi^2_{BS} = 9.00 \pm 3.45$, and for IR were $\chi^2_{AFI} = 1.44 \pm 0.42$, $\chi^2_{BS} = 2.44 \pm 1.21$. These results demonstrate the robustness of VFA for qMT F, even in the presence of local inaccuracies acquired in similar B_1 maps, and that B_1 maps containing minor artifacts can be used without degradation in quantitative F value precision.

DISCUSSION

Our findings demonstrate that the B_1 -sensitivity of off-resonance MT-prepared SPGR qMT parameters is strongly influenced by the T_1 mapping method used. We showed that the robustness of the fitted qMT parameters is impacted by the choice between a B_1 -independent and a B_1 -dependent T_1 mapping method impacts. Overall, the pool-size ratio F was shown to be most robust against B_1 errors when VFA T_1 mapping is used. Using simulations, we found that a 10% overestimation in B_1 results in a 1.5% error in F if VFA is used for T_1 mapping. This B_1 -induced error in F was 15 times less than for B_1 -independent methods such as IR (23% error in F). Although possibly a counter-intuitive prediction, the increased robustness in F against errors in B_1 for a B_1 -dependent T_1 method is made possible due to other fitting parameters (particularly k_f) being more compatible to compensate the expected signal errors for this case. In vivo measurements were in agreement with our simulations;

the F maps fitted using the nominal flip angle assumption (B_1 inaccuracy ranging between -10% and 25%) and VFA T_1 -mapping correlated strongly with the case using a measured B_1 map ($\rho = 0.97$). Histogram comparisons of WM qMT F between three different B_1 mapping methods showed that VFA could result in four to five times better histogram matching (χ^2 values) in the presence of B_1 inaccuracies compared to IR.

Although most B_1 mapping methods are designed to be robust to common sources of potential artifacts (i.e., tissues with long T_1), there is no well-accepted gold standard method for accurately imaging B_1 . Our comparison between three well-accepted B_1 imaging methods showed that $\pm 10\%$ in voxel-wise differences between B_1 maps can be reasonably expected, resulting in inevitable B_1 inaccuracies regardless of which technique is chosen. In addition, B_1 maps are typically filtered with large blurring kernels ($\sim 10\text{mm}^3$) (17,34,35), because B_1 maps are expected to have a smoothly varying profile (36). In the presence of local highly inaccurate voxels, blurring filters can have the unintended effect of biasing nearby voxels. Blurring filters can also be less effective in cortical grey matter due to edge effects, an area that is already sensitive to inaccuracies due to partial volume effects with CSF. Resampling low-resolution B_1 maps for higher resolution qMT applications means that some inaccurate

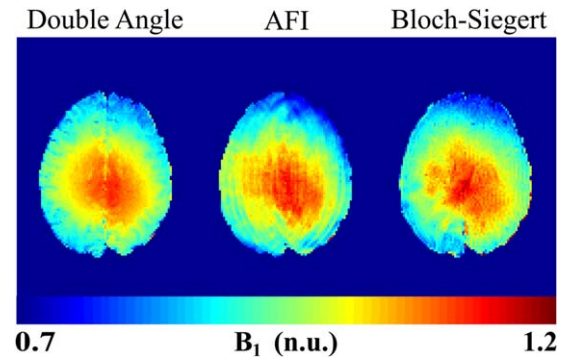


FIG. 7. B_1 map comparison in a single subject using three different acquisition techniques: double angle method, actual flip angle imaging (AFI), and Bloch-Siebert shift. n.u. = normalized units.

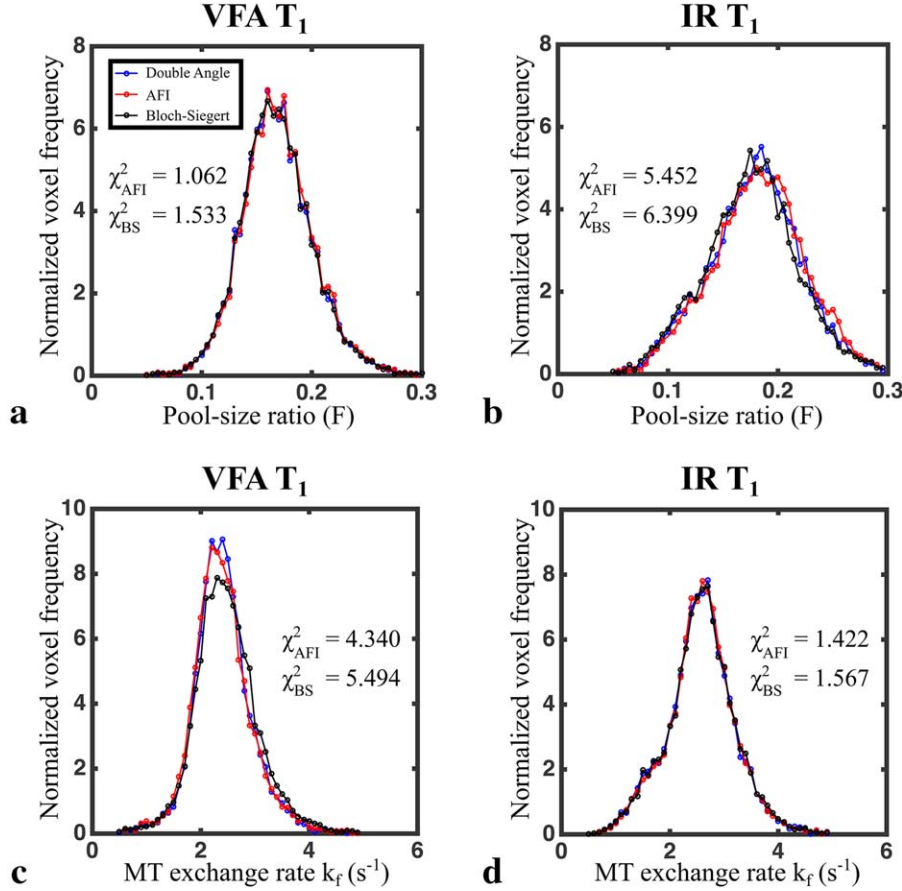


FIG. 8. Single-subject white matter pool-size (F) (a, b) and magnetization transfer (MT) exchange coefficient (k_f) (c, d) distributions for three B₁ mapping methods, using inversion recovery (IR) T₁ mapping (a, c) or variable flip angle (VFA) T₁ mapping (b, d). χ^2 values of the actual flip angle (AFI) and Bloch-Siebert shift (BS) histograms were calculated relative to double angle.

B₁ information will inevitably be used in qMT postprocessing. Overall, some inaccuracies in B₁ maps must be considered when planning the qMT acquisition protocol to minimize the sensitivity of the qMT parameter(s) of interest to this source of error.

The B₁-sensitivity characteristics reported here are limited to the qMT imaging method and model that were used. Several other qMT techniques could benefit from a similar analysis; well-established pulsed SPGR qMT alternatives include the Ramani (12) and the Yarnykh (11) models. A key difference between these three MT models is in how they approximate the MT pulse power (25). As B₁ is primarily used as a corrective factor for the MT pulse power, B₁-sensitivity will likely vary between these methods and could be explored in future work. Our sensitivity analysis results may also suggest that the B₁-sensitivity will vary depending on certain key Z-spectrum acquisition choices, particularly dependent on how many MT powers are used. The number of MT powers is conventionally limited to two; however, optimized acquisition schemes have used anywhere between one (33,37) and eight MT pulse powers (14).

Despite the fact that VFA T₁ mapping benefits qMT by improving the robustness of F, even for the extreme case of no B₁ correction at all, certain limitations must be carefully taken into consideration prior to integration into a protocol. As shown with simulations and in vivo, the increase in robustness of one qMT parameter for a certain choice of T₁ method (e.g., IR or VFA)

results in a reduction in robustness of the other fitted parameters. For instance, a study whose aim is to compare all the qMT parameters should refrain from omitting B₁ mapping, even if VFA is used, as k_f will be inaccurate in several regions. Accurate T₁ maps, which are valuable to many studies because they correlate with disease characteristics, would also be compromised if measuring B₁ is omitted in a qMT protocol that uses VFA. However, for circumstances where the certain qMT parameters have been well-characterized for the disease of interest (e.g., multiple sclerosis), choosing to improve the accuracy and robustness of one parameter (e.g., F) at the expense of others may be justified. Reducing the number of measurements to benefit one qMT parameter at the expense of others has been reported previously; for example, constraining multiple fitting parameters was used to achieve a single off-resonance qMT measurement technique of the pool-size ratio (33,37).

CONCLUSION

In summary, our work revealed the strong dependency of qMT B₁-sensitivity on the choice of T₁ mapping. Choosing carefully between a B₁-independent and B₁-dependent T₁ mapping method can greatly improve the precision of certain qMT parameters. Our results showed that, for a pulsed SPGR qMT sequence with uniform Z-spectrum sampling, using VFA T₁ mapping is preferable if the parameter of interest is the pool-size ratio F

parameter. The robustness against B₁ inaccuracy is so strong for this case, that B₁ mapping could be omitted altogether without resulting in large differences in fitted qMT F maps. Omitting this measurement could help accelerate lengthy qMT acquisition protocols, at the expense of losing quantitative T₁ information. B₁-sensitivity of qMT could be further improved by optimizing the Z-spectrum sampling scheme, similar to how qMT acquisition schemes have been optimized for noise performance (14).

APPENDIX A—SENSITIVITY ANALYSIS EQUATIONS

Let us assume an experiment consisting of N measurements $M_{i,\text{meas}}$ ($i = 1, 2, \dots, N$). Fitting the data to a mathematical model, the algorithm is expected converge to a state where $|M_{i,\text{meas}} - M_{i,\text{fit}}|$ is minimized at each point, such that ideally:

$$\begin{pmatrix} M_{1,\text{fit}}(p_1, \dots, p_L) \\ \vdots \\ M_{N,\text{fit}}(p_1, \dots, p_L) \end{pmatrix} \cong \begin{pmatrix} M_{1,\text{meas}} \\ \vdots \\ M_{N,\text{meas}} \end{pmatrix} \quad [\text{A1}]$$

$M_{i,\text{fit}}$ depends on a set model parameters p_k ($k = 1, 2, \dots, L$). For a small error in an measured model parameter $\Delta p_{j,\text{meas}}$ (i.e., a calibration measurement, such as B₁ in qMT), the change in each $M_{i,\text{fit}}$ is approximated by a Taylor expansion:

$$M_{i,\text{fit}}(p_{j,\text{meas}} + \Delta p_{j,\text{meas}}) = M_{i,\text{fit}}(p_{j,\text{meas}}) + \sum_{k=1}^L \frac{\partial M_{i,\text{fit}}}{\partial p_k} \Delta p_k + \dots \quad [\text{A2}]$$

The fitting algorithm will nonetheless aim at producing a good fit (Eq. [A1]); thus, the following approximations are expected:

$$M_{i,\text{fit}}(p_{j,\text{meas}} + \Delta p_{j,\text{meas}}) \cong M_{i,\text{meas}} \equiv M_i \quad [\text{A3}]$$

$$M_{i,\text{fit}}(p_{j,\text{meas}}) \cong M_{i,\text{meas}} \equiv M_i \quad [\text{A4}]$$

A first order approximation of the Taylor series for small $\Delta p_{j,\text{meas}}$ and substituting for M_i condenses Eq. [A2] to:

$$M_i \cong M_i + \sum_{k=1}^L \frac{\partial M_i}{\partial p_k} \Delta p_k \quad [\text{A5}]$$

The M_i terms cancel, thus any error caused by $\Delta p_{j,\text{meas}}$ must be compensated by errors propagated to the remaining fitting parameters Δp for $k \neq j$:

$$\sum_{k=1, k \neq j}^L \frac{\partial M_i}{\partial p_k} \Delta p_k = - \frac{\partial M_i}{\partial p_{j,\text{meas}}} \Delta p_{j,\text{meas}} \quad [\text{A6}]$$

For the Sled and Pike model of qMT, the calibration measurement we are interested in as a possible source of error in this work is B₁, and the explicitly fitted parameters are F, k_f, T_{2f} and T_{2r}:

$$\frac{\partial M_i}{\partial F} \Delta F + \frac{\partial M_i}{\partial k_f} \Delta k_f + \frac{\partial M_i}{\partial T_{2f}} \Delta T_{2f} + \frac{\partial M_i}{\partial T_{2r}} \Delta T_{2r} = - \frac{\partial M_i}{\partial B_1} \Delta B_1 \quad [\text{A7}]$$

The sensitivity of a measurement M_i relative to a model parameter p_k is defined as (27):

$$S_{p_k,i} \equiv \frac{\partial M_i}{\partial p_k} \quad [\text{A8}]$$

For a set of N measurements, Eqs. [A7] and [A8] simplify to matrix form:

$$\begin{pmatrix} S_{F,1} & S_{k_f,1} & S_{T_{2f},1} & S_{T_{2r},1} \\ S_{F,2} & S_{k_f,2} & S_{T_{2f},2} & S_{T_{2r},2} \\ \vdots & \vdots & \vdots & \vdots \\ S_{F,N} & S_{k_f,N} & S_{T_{2f},N} & S_{T_{2r},N} \end{pmatrix} \begin{pmatrix} \Delta F \\ \Delta k_f \\ \Delta T_{2f} \\ \Delta T_{2r} \end{pmatrix} = - \begin{pmatrix} S_{B_1,1} \\ S_{B_1,2} \\ \vdots \\ S_{B_1,N} \end{pmatrix} \Delta B_1 \quad [\text{A10}]$$

For a given error in B₁ (ΔB_1), Eq. [A10] could be minimized to estimate the errors in each fitting parameter (ΔF , Δk_f , ΔT_{2f} , ΔT_{2r}) having known sensitivity values, which can be calculated analytically or through numerical simulations. However, to simplify the analysis, we chose to compare each fitting parameter p_k independently to find possible easy-to-understand metrics to compare fitting parameter sensitivity to B₁ inaccuracies. For each fitting parameter of interest (Δp), we set all other Δp_k values to 0. Equation [A10] now simplifies to a vector equation:

$$\mathbf{S}_p \Delta p = -\mathbf{S}_{B_1} \Delta B_1 \quad [\text{A11}]$$

where \mathbf{S}_p is the column vector for the parameter of interest p in Equation [A10], similar to \mathbf{S}_{B_1} . This equation is solved for Δp by doing the scalar product of \mathbf{S}_p on both sides of the equation, and separating the norm of the vectors $\|\mathbf{s}\|$ and their unit vectors ($\hat{\mathbf{S}}$). Also, because Δp and ΔB_1 are absolute errors, they are scaled by the parameter values ($\Delta p = p \delta p$, where δp is the relative error). To better compare each parameter, the relative error is preferred:

$$\delta p = - \frac{B_1}{p} \frac{\|\mathbf{S}_{B_1}\|}{\|\mathbf{S}_p\|} (\hat{\mathbf{S}}_p \cdot \hat{\mathbf{S}}_{B_1}) \delta B_1 \quad [\text{A12}]$$

Thus, for a given relative error in B₁ (δB_1), the parameter p , which maximizes $|\hat{\mathbf{S}}_p \cdot \hat{\mathbf{S}}_{B_1}|$ for a given measurement protocol, will likely have larger inaccuracies $|\delta p|$ than the other fitting parameters. This can be visualized easily, because $|\hat{\mathbf{S}}_p \cdot \hat{\mathbf{S}}_{B_1}| \approx 1$ means that the sensitivity curves for B₁ and p nearly match, and any change in the Z-spectrum expected by an inaccurate B₁ can be nearly completely compensated solely by adjusting that fitting parameter. The error induced (δp) will then proportional to the ratio of overall sensitivities $\frac{B_1}{p} \frac{\|\mathbf{S}_{B_1}\|}{\|\mathbf{S}_p\|}$.

ACKNOWLEDGMENTS

Funding for M.B. was provided by the National Sciences and Engineering Research Council of Canada with the Alexander Graham Bell Canada Graduate Scholarships—

Doctoral program. Funding to G.B.P. was provided by the Canadian Institutes of Health Research, and Campus Alberta Innovates Program also supported this research.

REFERENCES

- Wolff SD, Balaban RS. Magnetization transfer contrast (MTC) and tissue water proton relaxation in vivo. *Magn Reson Med* 1989;10:135–144.
- Henkelman RM, Huang X, Xiang QS, Stanisz GJ, Swanson SD, Bronskill MJ. Quantitative interpretation of magnetization transfer. *Magn Reson Med* 1993;29:759–766.
- Schmierer K, Tozer DJ, Scaravilli F, Altmann DR, Barker GJ, Tofts PS, Miller DH. Quantitative magnetization transfer imaging in postmortem multiple sclerosis brain. *J Magn Reson Imaging* 2007;26:41–51.
- Schmierer K, Wheeler-Kingshott CAM, Tozer DJ, Boulby PA, Parkes HG, Yousry TA, Scaravilli F, Barker GJ, Tofts PS, Miller DH. Quantitative magnetic resonance of postmortem multiple sclerosis brain before and after fixation. *Magn Reson Med* 2008;59:268–277.
- Tozer D, Ramani A, Barker GJ, Davies GR, Miller DH, Tofts PS. Quantitative magnetization transfer mapping of bound protons in multiple sclerosis. *Magn Reson Med* 2003;50:83–91.
- Davies GR, Tozer DJ, Cercignani M, Ramani A, Dalton CM, Thompson AJ, Barker GJ, Tofts PS, Miller DH. Estimation of the macromolecular proton fraction and bound pool T2 in multiple sclerosis. *Mult Scler* 2004;10:607–613.
- Levesque IR, Giacomini PS, Narayanan S, Ribeiro LT, Sled JG, Arnold DL, Pike GB. Quantitative magnetization transfer and myelin water imaging of the evolution of acute multiple sclerosis lesions. *Magn Reson Med* 2010;63:633–640.
- Gloor M, Scheffler K, Bieri O. Quantitative magnetization transfer imaging using balanced SSFP. *Magn Reson Med* 2008;60:691–700.
- Dortch RD, Li K, Gochberg DF, Welch EB, Dula AN, Tamhane AA, Gore JC, Smith SA. Quantitative magnetization transfer imaging in human brain at 3 T via selective inversion recovery. *Magn Reson Med* 2011;66:1346–1352.
- Sled JG, Pike GB. Quantitative interpretation of magnetization transfer in spoiled gradient echo MRI sequences. *J Magn Reson* 2000;145:24–36.
- Yarnykh VL. Pulsed Z-spectroscopic imaging of cross-relaxation parameters in tissues for human MRI: theory and clinical applications. *Magn Reson Med* 2002;47:929–939.
- Ramani A, Dalton C, Miller DH, Tofts PS, Barker GJ. Precise estimate of fundamental in-vivo MT parameters in human brain in clinically feasible times. *Magn Reson Imaging* 2002;20:721–731.
- Pike GB. Pulsed magnetization transfer contrast in gradient echo imaging: a two-pool analytic description of signal response. *Magn Reson Med* 1996;36:95–103.
- Levesque IR, Sled JG, Pike GB. Iterative optimization method for design of quantitative magnetization transfer imaging experiments. *Magn Reson Med* 2011;66:635–643.
- Cercignani M, Symms MR, Schmierer K, Boulby PA, Tozer DJ, Ron M, Tofts PS, Barker GJ. Three-dimensional quantitative magnetisation transfer imaging of the human brain. *NeuroImage* 2005;27:436–441.
- Underhill HR, Yuan C, Yarnykh VL. Direct quantitative comparison between cross-relaxation imaging and diffusion tensor imaging of the human brain at 3.0 T. *Neuroimage* 2009;47:1568–1578.
- Yarnykh VL. Actual flip-angle imaging in the pulsed steady state: a method for rapid three-dimensional mapping of the transmitted radiofrequency field. *Magn Reson Med* 2007;57:192–200.
- Sacolic LI, Wiesinger F, Hancu I, Vogel MW. B1 mapping by Bloch-Siegert shift. *Magn Reson Med* 2010;63:1315–1322.
- Yarnykh VL. Optimal radiofrequency and gradient spoiling for improved accuracy of T1 and B1 measurements using fast steady-state techniques. *Magn Reson Med* 2010;63:1610–1626.
- Barral JK, Gudmundson E, Stikov N, Etezadi-Amoli M, Stoica P, Nishimura DG. A robust methodology for in vivo T1 mapping. *Magn Reson Med* 2010;64:1057–1067.
- Stikov N, Boudreau M, Levesque IR, Tardif CL, Barral JK, Pike GB. On the accuracy of T1 mapping: searching for common ground. *Magn Reson Med* 2015;73:514–522.
- Liberman G, Louzoun Y, Ben Bashat D. T(1) mapping using variable flip angle SPGR data with flip angle correction. *J Magn Reson Imaging* 2014;40:171–180.
- Sled JG, Pike GB. Quantitative imaging of magnetization transfer exchange and relaxation properties in vivo using MRI. *Magn Reson Med* 2001;46:923–931.
- Levesque IR, Chia CL, Pike GB. Reproducibility of in vivo magnetic resonance imaging-based measurement of myelin water. *J Magn Reson Imaging* 2010;32:60–68.
- Portnoy S, Stanisz GJ. Modeling pulsed magnetization transfer. *Magn Reson Med* 2007;58:144–155.
- Fram EK, Herfkens RJ, Johnson GA, Glover GH, Karis JP, Shimakawa A, Perkins TG, Pelc NJ. Rapid Calculation of T1 Using Variable Flip Angle Gradient Refocused Imaging. *Magn Reson Imaging* 1987;5:201–208.
- Cruz JB. System Sensitivity Analysis. Stroudsburg, PA: Dowden, Hutchinson & Ross; 1973.
- Grad J, Mendelson D, Hyder F, Bryant RG. Applications of nuclear magnetic cross-relaxation spectroscopy to tissues. *Magn Reson Med* 1991;17:452–459.
- Skinner TE, Glover GH. An extended two-point Dixon algorithm for calculating separate water, fat, and B0 images. *Magn Reson Med* 1997;37:628–630.
- Cabana J-F, Gu Y, Boudreau M, et al. Quantitative magnetization transfer imaging made easy with qMTLab: software for data simulation, analysis, and visualization. *Concepts Magn Reson Part A* 2015;44A:263–277.
- Lutti A, Stadler J, Josephs O, Windischberger C, Speck O, Bernarding J, Hutton C, Weiskopf N. Robust and fast whole brain mapping of the RF transmit field B1 at 7T. *PLoS One* 2012;7:e32379.
- Collins DL, Zijdenbos A, Baaré WC, Evans A. ANIMAL+INSECT: improved cortical structure segmentation. In: Kuba A, Šámal M, Todd-Pokropek A, eds. *Information Processing in Medical Imaging*. Vol. 1613, Lecture Notes in Computer Science. Berlin-Heidelberg, Germany: Springer; 1999:210–223.
- Yarnykh VL. Fast macromolecular proton fraction mapping from a single off-resonance magnetization transfer measurement. *Magn Reson Med* 2012;68:166–178.
- Helms G, Finsterbusch J, Weiskopf N, Dechent P. Rapid radiofrequency field mapping in vivo using single-shot STEAM MRI. *Magn Reson Med* 2008;60:739–743.
- Lutti A, Hutton C, Finsterbusch J, Helms G, Weiskopf N. Optimization and validation of methods for mapping of the radiofrequency transmit field at 3T. *Magn Reson Med* 2010;64:229–238.
- Sled JG, Zijdenbos AP, Evans AC. A nonparametric method for automatic correction of intensity nonuniformity in MRI data. *IEEE Trans Med Imaging* 1998;17:87–97.
- Underhill HR, Rostomily RC, Mikheev AM, Yuan C, Yarnykh VL. Fast bound pool fraction imaging of the in vivo rat brain: association with myelin content and validation in the C6 glioma model. *Neuroimage* 2011;54:2052–2065.